ROYAL SOCIETY
OF CHEMISTRY

PAPER

Check for updates

Nanoallotrope-integrated polyacrylamide hydrogels: a synergistic experiment–theory approach for engineering mechanically resilient and cytocompatible composites for cartilage tissue regeneration

Nehal,[a] Murli Manohar,[b] Komal,*[a] Kantesh Balani, [ID] *[b] Sarvesh Kumar Pandey*[c] and Shikha Awasthi [ID] *[d]

Polyacrylamide (PAM)-based hydrogels are commonly acknowledged as promising contenders for replacing cartilage. Nevertheless, their restricted mechanical strength and puncture resistance greatly impeded their ability to be used in biological applications. The current investigation aimed to increase the strength of polyacrylamide hydrogels by including carbon nanotubes (CNTs) and graphene oxide (GO) in various concentrations in a PAM matrix. Combining CNT and GO nanoparticles with PAM results in a synergistic effect and a strong interfacial bonding. This leads to high compressive strength and elastic modulus. The PAM–CNT and PAM–GO composite hydrogels exhibited remarkable self-healing characteristics, bioactivity, and cytocompatibility. This was evidenced by a cell survival rate of over 99%. The incorporation of GO markedly improved the hydrophilicity of the composites, resulting in a contact angle of 40°. The swelling characteristics of the hydrogels were assessed, revealing that PAM–GO1 (0.3 g L^{-1}) and PAM–GO2 (0.5 g L^{-1}) exhibited the greatest stability. *In vitro* degradation tests showed that both PAM–GO1 (0.3 g L^{-1}) and PAM–GO2 (0.5 g L^{-1}) preserved approximately 90% of their gel mass following 20 days of immersion in PBS. Compression tests revealed that PAM–GO1 (0.3 g L^{-1}) has the greatest compressive strength ($\approx$0.31 MPa) and highest elastic modulus (1.653 MPa). Furthermore, the PAM–GO hydrogels demonstrated exceptional cell survival, almost surpassing 100%. The best antimicrobial activity was found in PAM–GO1. In attaining new insights into the structural [interfacial interactions recognized by the noncovalent interactions (NCIs) and van der Waals (vdW) interactions], stability/strength, energetic [binding energy (BE)], and electronic [HOMO–LUMO gap and charge transfer (CT)] features of both composites, an *in-silico* approach has been applied. The PAM–GO composite model was found to be more stable than the PAM–CNTCOOH composite model. The BE, HOMO–LUMO gap, some selected QTAIM-based parameters, dipole moment, and CT-related parameters supported the experiment-based outcomes. In summary, the PAM–GO1 (0.3 g L^{-1}) hydrogel composite, characterized by enhanced mechanical characteristics, bioactivity, and robust adhesion, has considerable potential as an advanced hydrogel material for cartilage repair applications.

*aDepartment of Chemistry, Manipal University Jaipur, Jaipur-303007, India.
E-mail: komal.arora@jaipur.manipal.edu*
*bDepartment of Materials Science and Engineering, IIT, Kanpur-208016, India.
E-mail: kbalani@iitk.ac.in*
*cDepartment of Chemistry, Maulana Azad National Institute of Technology,
Bhopal-462003, Madhya Pradesh, India. E-mail: sarvesh@manit.ac.in*
*dDepartment of Basic Sciences, IES College of Technology, Bhopal-462044,
Madhya Pradesh, India. E-mail: awas.shikha2212@gmail.com*

1. Introduction

Hydrogels are flexible polymers that are well known for their exceptional ability to interact well with living organisms and store a large amount of water due to their complex three-dimensional network structure. They can create blends by combining several monomers and cross-linkers. Hydrogels have been infused with different biocompatible substances to create hydrogel composites, which have been examined for novel uses.[1–4] While natural hydrogels such as alginate, gelatin, and chitosan offer excellent biocompatibility, they

suffer from poor mechanical strength and unpredictable degradation rates.[5] Synthetic hydrogels, on the other hand, offer a tunable crosslinking density, chemical functionality, and mechanical stability, making them favourable for applications requiring structural robustness.[6,7]

Among synthetic hydrogels, polyacrylamide (PAM) has emerged as a versatile candidate because of its hydrophilic nature, transparency, non-toxicity, and mechanical flexibility.[8] PAM chains contain amide groups capable of forming hydrogen bonds and interacting with other functional moieties, making them suitable for blending or reinforcement.[9] The viscoelastic properties of PAM hydrogels allow them to exhibit both solid-like and fluid-like behaviours, a feature advantageous for simulating the mechanical environment of cartilage or soft tissues.[10] Despite these advantages, pristine PAM hydrogels are mechanically weak, brittle under compression, and often lack sufficient bioactivity for cell proliferation and differentiation. Consequently, strategies to enhance their mechanical resilience and biocompatibility have become central to recent research efforts.[11,12]

One of the most promising routes to strengthen hydrogels involves incorporating nanoscale fillers that can create additional physical or chemical crosslinks within the polymer network. Nanocomposite hydrogels combine the softness and water content of traditional hydrogels with the toughness and functional versatility of nanomaterials.[13] Carbon-based nanomaterials, particularly carbon nanotubes (CNTs) and graphene oxide (GO), have attracted widespread attention for this purpose. CNTs are known for their exceptional tensile strength and one-dimensional morphology, while GO, with its two-dimensional layered structure, provides abundant oxygenated functional groups (–COOH, –OH, –C=O) that promote hydrogen bonding and electrostatic interactions with polymer chains.[14,15] These interactions not only improve dispersion, but also enhance the load transfer efficiency across the polymer–nanofiller interface, thereby reinforcing the hydrogel matrix.[16]

Although both CNT- and GO-reinforced PAM hydrogels have been individually explored, comparative analyses of their structural and biological performances remain scarce. Furthermore, most experimental studies lack theoretical validation that can reveal how molecular-level interactions influence macroscopic behavior. Integrating computational modeling with experimental data provides valuable insight into binding energies, charge transfer mechanisms, and interfacial stability, which are often difficult to probe through experiments alone. In the present work, PAM-based hydrogels reinforced with CNTs and GO were synthesized using free radical polymerization to develop mechanically robust, cyto-compatible, and bioactive scaffolds for cartilage tissue regeneration. Various concentrations of CNTs and GO were evaluated to determine optimal reinforcement levels. Structural (FTIR, XRD, SEM), mechanical, and biological assessments were conducted to characterize the composite performance. To support the strength and stability-based experimental outcomes, the structural, stability, and electronic feature analyses have been

reported in the current research work for a range of useful and interesting quantum chemical calculation-based parameters, which especially portray the interfacial [H-bonding and other weak van der Waals (vdW)] interactions taking part between the two constituting components of the two proposed composite models (PAM-GO and PAM-CNTCOOH). For instance, a variety of chemical species existing in the form of complexes have been reported in the literature, including a range of interesting composite models.[17–19] This synergistic experiment–theory approach provides a comprehensive understanding of nanoallotrope–polymer interactions, enabling the rational design of next-generation hydrogels for regenerative medicine and related biomedical applications.

2. Materials and methods

2.1 Experimental studies

2.1.1. Preparation of hydrogel composites. The polyacrylamide hydrogel (PAM) was produced by carrying out a free radical polymerization process with the acrylamide monomer. The catalysts used in the process were ammonium persulfate and tetramethylethylenediamine, whereas the cross-linker employed was N,N'-methylene bisacrylamide.[20] Table 1 contains information on the amounts of the substances utilized and the nomenclature of the samples. Carbon nanotubes with a diameter of 30–50 nm and 95% purity were purchased from Nanostructured and Amorphous Materials Inc. in the United States. Graphene oxide (Tokyo Chemical Industry, TCI, average size: 6–14 mm) was purchased from Sarthak Sales Pvt. Ltd, Jaipur, India. The pure carbon nanotubes (400 mg) were evenly distributed in a solution of sulfuric acid and nitric acid (3 : 1) using ultrasonic waves for roughly 7 h. The resulting solid was subsequently filtered, rinsed with deionized water, and dried at 80 °C for one day. The functionalized carbon nanotubes (CNTs) were modified with carboxylic groups, leading to enhanced dispersibility in water. The PAM hydrogel sections were dried and then submerged in separate solutions of CNTs and GO, each containing 100 mL, for 48 h. Subsequently, the composite hydrogels were immersed in distilled water for 24 h to eliminate any surplus bound ions present on the polyacrylamide hydrogel's surface. Thus, seven types of samples were prepared as pure PAM, PAM with CNTs (0.3 g L^{-1}, 0.5 g L^{-1}, 0.7 g L^{-1}), and PAM with GO (0.3 g L^{-1}, 0.5 g L^{-1}, 0.7 g L^{-1}).

2.1.2 Physicochemical characterization of hydrogels. The materials were observed for their top surface morphology using the Karl Zeiss Ultra 55 FE-SEM scanning electron microscope. The materials were analyzed using an X-ray diffractometer (Rigaku SmartLab) with a Cu Kα wavelength λ of 1.5417 Å in the 2θ range from 10 to 80° to determine the phases present. The testing was conducted using a scan rate of 3° min^{-1} and a scan step size of 0.02°. Moreover, the interaction between the nanoparticles and the polymeric network may be demonstrated by the existing functional groups. To achieve this objective, Fourier transform infrared (FTIR) spec-

Table 1 Chemical composition and nomenclature of the hydrogel composites

Description of samples	Nomenclature	Chemical composition
Polyacrylamide hydrogels	PAM	Acrylamide: 10 g; N,N'-methylene: 0.266 g bisacrylamide; ammonium persulphate: 0.20 g; tetramethylethylenediamine:610.14 μL
Polyacrylamide hydrogels with CNTs	PAM–CNT1	PAM (acrylamide: 10 g; N,N'-methylene: 0.266 g bisacrylamide; ammonium persulphate: 0.20 g; tetramethylethylenediamine:610.14 μL) + CNT: 0.3 g L^{-1}
	PAM–CNT2	PAM (acrylamide: 10 g; N,N'-methylene: 0.266 g bisacrylamide; ammonium persulphate: 0.20 g; tetramethylethylenediamine: 610.14 μL) + CNT-0.5 g L^{-1}
	PAM–CNT3	PAM (acrylamide: 10 g; N,N'-methylene: 0.266 g bisacrylamide; ammonium persulphate: 0.20 g; tetramethylethylenediamine: 610.14 μL) + CNT: 0.7 g L^{-1}
Polyacrylamide hydrogels with GO	PAM–GO1	PAM (acrylamide: 10 g; N,N'-methylene: 0.266 g bisacrylamide; ammonium persulphate: 0.20 g; tetramethylethylenediamine: 610.14 μL) + GO-0.3 g L^{-1}
	PAM–GO2	PAM (acrylamide: 10 g; N,N'-methylene: 0.266 g bisacrylamide; ammonium persulphate: 0.20 g; tetramethylethylenediamine: 610.14 μL) + GO-0.5 g L^{-1}
	PAM–GO3	PAM (acrylamide: 10 g; N,N'-methylene: 0.266 g bisacrylamide; ammonium persulphate: 0.20 g; tetramethylethylenediamine: 610.14 μL) + GO-0.7 g L^{-1}

troscopy was utilized in the wavenumber range of 500–4000 cm^{-1}.

2.1.3 Swelling, contact angle, and degradation behaviour *in vitro*. The hydrophilicity of the hydrogel surface was determined using a Dataphysics TC/TEC 400 contact angle goniometer. Measurements were performed in triplicate at different sample locations, and the mean value was reported (n = 3). A 5 μL drop of phosphate buffer saline (PBS) with a pH of 7.4 was utilized to determine the contact angle on the samples. The swelling properties of pure PAM and PAM-based composite hydrogels were assessed by measuring the initial mass of the samples, and then immersing the hydrogels in 100 mL of PBS (pH 7.4) at 37 °C for 24 h until they achieved a state of swelling equilibrium. The enlarged hydrogels were measured at various time intervals (2, 5, 10, 15, 20, and 25 h) to determine their weight. The swelling rate (SR) was calculated using the equation:

$$SR = \frac{W_s - W_i}{W_i} \tag{1}$$

where W_s and W_i are the weights of the hydrogel at equilibrium swelling and in the initial state, respectively. In addition, the degradation behaviour of the hydrogels was assessed by measuring the mass of the samples after 48 h in PBS. After attaining equilibrium swelling, the samples started to deteriorate, and the residual mass of the hydrogels was measured at certain time intervals (up to 20 days). The percentage of the gel's residual mass was determined using the following equation.

$$\text{Remaining gel } (\%) = \frac{W_0 - W_t}{W_0} \times 100 \tag{2}$$

where W_0 and W_t are the weights of hydrogels after 48 h and after time t, respectively. All measurements were performed in triplicate (n = 3), and results are presented as mean ± standard deviation (SD).

2.1.4 Compression test. A compression test was performed on samples measuring 10 mm in diameter and 10 mm in height using universal testing equipment manufactured by Magnum Pvt. Ltd in India. The compression was consistently delivered at a rate of 3.33 mm per minute. All measurements were performed in triplicate (n = 3), and results are presented as mean ± standard deviation (SD).

2.1.5 Cytotoxicity measurement. The cytocompatibility of the hydrogels was assessed through the MTT assay (3-(4,5-dimethylthiazol-2-yl)-2,5-diphenyltetrazolium bromide) to determine MG-63 cell viability and was further evaluated by fluorescence microscopy to observe the cell morphology. MG-63 cells were grown into 24-well plates (on the cover slip) in high-glucose DMEM supplemented with 10% FBS and 1% penicillin–streptomycin. The cells were then incubated for 24 hours at 37 °C in an atmosphere with 5% CO$_2$ and 80–90% humidity. Under the same circumstances, the hydrogel samples were simultaneously submerged in full medium and given a 24-hour period to swell. After 24 hours of incubation swelled samples were transferred in the cell grown 24 well plates and then incubated for 72 hours.

MTT testing. Following 72 hours of incubation, each well was cleaned twice with 1XPBS before the MTT reagent was applied. To facilitate the development of insoluble formazan crystals, the cells were subsequently incubated for three hours at 37 °C. After carefully removing the MTT solution, DMSO was added in an equal amount to each well so that the sample could be submerged and the formazan crystals would dissolve during the course of ten to fifteen minutes of incubation. Cell viability was assessed by transferring the resultant solution to a 96-well plate and using a microplate reader to measure the optical density (OD) at 570 nm.

$$\text{Cell viability } (\%) = \frac{\text{OD\_test} - \text{OD\_blank}}{\text{OD\_control} - \text{OD\_blank}} \times 100 \tag{3}$$

OD_test, OD_blank, and OD_control represent the optical densities of cells incubated with hydrogels, medium devoid of cells, and media containing cells, respectively.

Fluorescence microscopy. Following 72 hours of incubation, each well was cleaned twice with 1×PBS before the samples were fixed in 4% paraformaldehyde (PFA) for 45–55 minutes at 4 °C after incubation. They were then gently washed twice with phosphate-buffered saline (1XPBS), permeabilized with 0.1% Triton X-100 for 8–12 minutes (at room temperature), and then

washed twice more with PBS for fluorescence microscopy. Cells were treated with 1% bovine serum albumin (BSA) for 45–55 minutes in order to prevent non-specific binding. The actin cytoskeleton was stained with Alexa Fluor 488 conjugated phalloidin for 45–50 minutes in the dark after being rinsed twice with 1XPBS. This was followed by 10-minute nuclear staining with DAPI (4′,6-diamidino-2-phenylindole). Samples were examined using FITC and UV-2A filter sets, scale bar = 25 μm, following a final PBS wash.

2.1.6 Antimicrobial analysis of hydrogels. *E. coli* (MTCC: 443) and *S. aureus* (MTCC: 3160) were used to evaluate samples' antibacterial effectiveness. Both the bacterial strains were cultured and incubated overnight to obtain healthy grown bacteria. Before seeding, samples were sterilized by autoclaving, cleaning with ethanol for 20 minutes under UV exposure, and rinsing with 1XPBS. Subsequently, samples were incubated for 24 h for complete swelling to avoid any further swelling. Each of the bacterial solutions (0.1 optical density) was seeded on the samples (10 g L^{-1} sample, triplicate samples tested three times) on a 24-well plate using 200 μL of suspension, followed by the addition of 700 μL of Luria broth (LB) medium to ensure complete immersion of the samples, and then incubated for 4 h. Following incubation, LB medium was substituted with the MTT reagent and incubated for an additional 2 h with prior washing twice with 1XPBS. The MTT reagent was substituted with DMSO (incubated for 10 minutes), without prior washing with PBS. The sample is subsequently transferred to a 96-well plate, and the optical density is measured at 570 nm using an ELISA plate reader.

2.1.7 Statistical analysis. Statistical analyses were performed using SPSS software (IBM). Analysis of variance (one-way ANOVA) was applied to evaluate the differences among experimental groups, followed by *post hoc* multiple comparisons using Tukey's and Games–Howell tests. A significance level of $p < 0.05$ was considered statistically meaningful.

2.1.8 Computational methodology. To achieve new insights and a better understanding of interfacial interactions involved in the two selected composite models (PAM–CNTCOOH and PAM–GO), an *in-silico* approach has been applied in the framework of *ab initio* [Hartree–Fock (HF)] and density functional theory (DFT) approaches using the Gaussian 16 electronic structure package installed on the Linux workstation. A total of five systems (three components, as the PAM, GO, and CNTCOOH, as well as two composite models as mentioned above) have been chosen for the optimization and frequency calculations, where all systems were found to be stable due to having all positive frequencies on the potential energy surface. All systems were optimized using the HF/3-21G method; however, due to both composite models consisting of a large size along with the availability of limited computational resources, only single point (SP) calculations were performed for all five species in the framework of the DFT approach (B3LYP/6-31G* level of theory). Natural population analysis (NPA) was also performed for both com-

posite models in the framework of the natural bond order (NBO) approach, followed by the DFT level of approach. A very popular quantum theory of atoms in molecules (QTAIM) tool was also used to gain deep insights into the nature, kind, and strength of the interfacial interactions engaged in both composite models, which facilitated noteworthy outcomes in terms of portraying the strength and stability of both composite systems in terms of highest occupied molecular orbital (HOMOs) and lowest unoccupied molecular orbitals (LUMOs) and their gaps including their three-dimensional HOMO and LUMO maps.[21,22]

3. Results and discussion

3.1. Physicochemical evaluation of hydrogels

Fig. 1 shows that the cross-sections of the hydrogels exhibit a smooth surface morphology, lacking any distinct features, in the case of pure PAM. Fig. 2 shows the embedded CNTs and GO particles within the PAM matrix.

After confirming the encapsulation of nanoparticles by the PAM gel, the preservation of phases in hydrogel hybrids was validated by XRD analysis (Fig. 3a). The pure polyacrylamide hydrogel (PAM) displays wide peaks, suggesting its lack of crystalline structure.[23] The XRD spectra of the PAM–CNT and PAM–GO hydrogels do not show peaks because carbon has low reflectivity in XRD, as seen in Fig. 3a.

The bonding between the composite hydrogels was verified using FT-IR spectroscopy (Fig. 3b). The O–H bond is responsible for a vibrational band at roughly 3601 cm^{-1}.[24] The stretching vibration band of the carbonyl group was detected at about 1526 cm^{-1}.[25] The band at 1702 cm^{-1} confirms the presence of amide functionalities in PAM.

3.2 Hydrophilicity of hydrogels, swelling, and degradation performance of the hydrogel composites

The hydrophilic behaviour of the hydrogel was assessed by quantifying the contact angles (Fig. 4). The contact angle of pure PAM was measured to be around 75°. The contact angles of the PAM–CNT composites (about 50°) showed improved hydrophilic properties due to the presence of hydrophilic –COOH functionalized CNTs. The incorporation of GO in the PAM hydrogel generated a heightened hydrophilic atmosphere, leading to a reduced contact angle of around 40° (Fig. 5). The hydrophilicity of a material is an essential attribute for biomedical implants since it can improve the adsorption of proteins and the reactions of cells in biological systems. In addition, hydrophilic implants can enhance the pace of bone growth.[26]

The compactness of the hydrogel network, surface area, and particle size can substantially affect the material's swelling rate.[27] Swelling analysis in phosphate-buffered saline (PBS) revealed that equilibrium was reached within 10 h for all samples (Fig. 5). PAM–GO1 and PAM–GO2 exhibited lower swelling ratios than PAM–CNT composites, reflecting denser polymer networks and efficient crosslinking provided by GO.
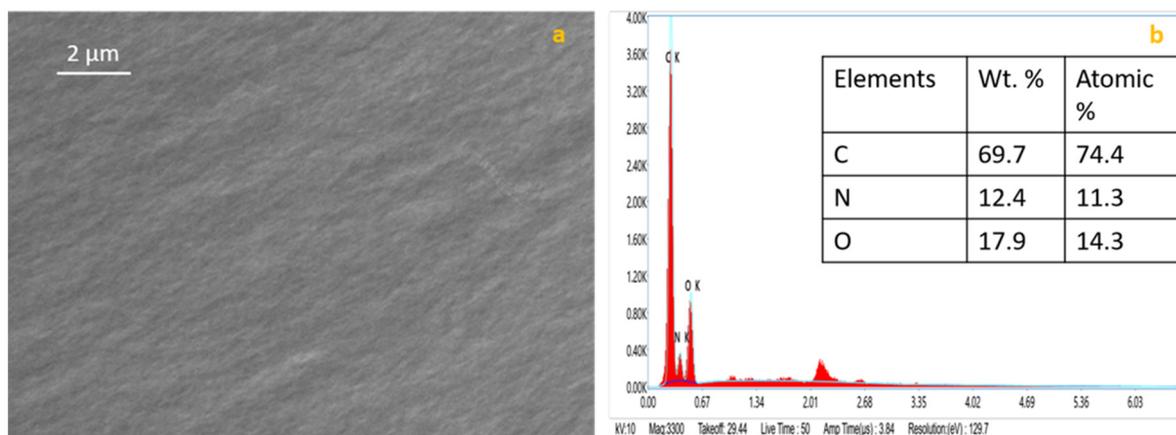
Fig. 1 (a) Scanning electron microscopy; (b) EDAX images of the cross-section of the pure PAM.
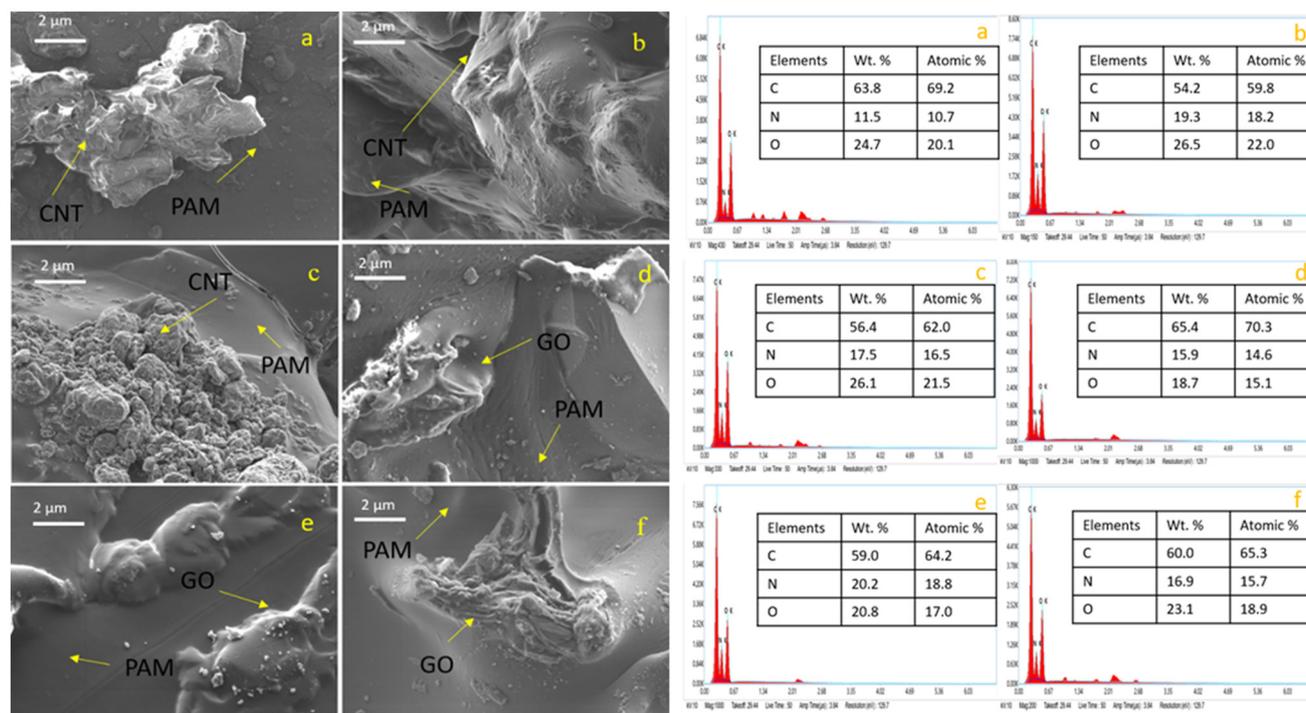

Fig. 2 Scanning electron microscopy images and EDAX on the cross-section of the (a) PAM–CNT1, (b) PAM–CNT2, (c) PAM–CNT3, (d) PAM–GO1, (e) PAM–GO2, and (f) PAM–GO3 hydrogel composites.

This controlled swelling behaviour is beneficial for maintaining mechanical stability and dimensional integrity in hydrated environments.[28] PAM–CNT degrades faster because CNTs provide weaker reinforcement, absorb more water, and can form aggregation-induced defects. Hence, PAM–GO is better suited for cartilage repair applications.

3.3 Compression test

The use of nanoparticles significantly increased compressive strength and elasticity, according to mechanical characterization

(Fig. 6). At about 69% strain, pure PAM broke and showed a compressive strength of 0.072 MPa. PAM–CNT2 and PAM–GO2 both attained strengths of approximately 0.14 and 0.19 MPa, respectively, whereas PAM–GO1 (0.3 g L^{-1}) achieved the maximum compressive strength of 0.31 MPa, withstanding over 90% strain without failure. The addition of nanofillers significantly increased mechanical resistance. Uniform GO dispersion and robust interfacial bonding, which facilitate effective load transmission, are responsible for this improvement. Agglomeration and mechanical degradation occur when loading
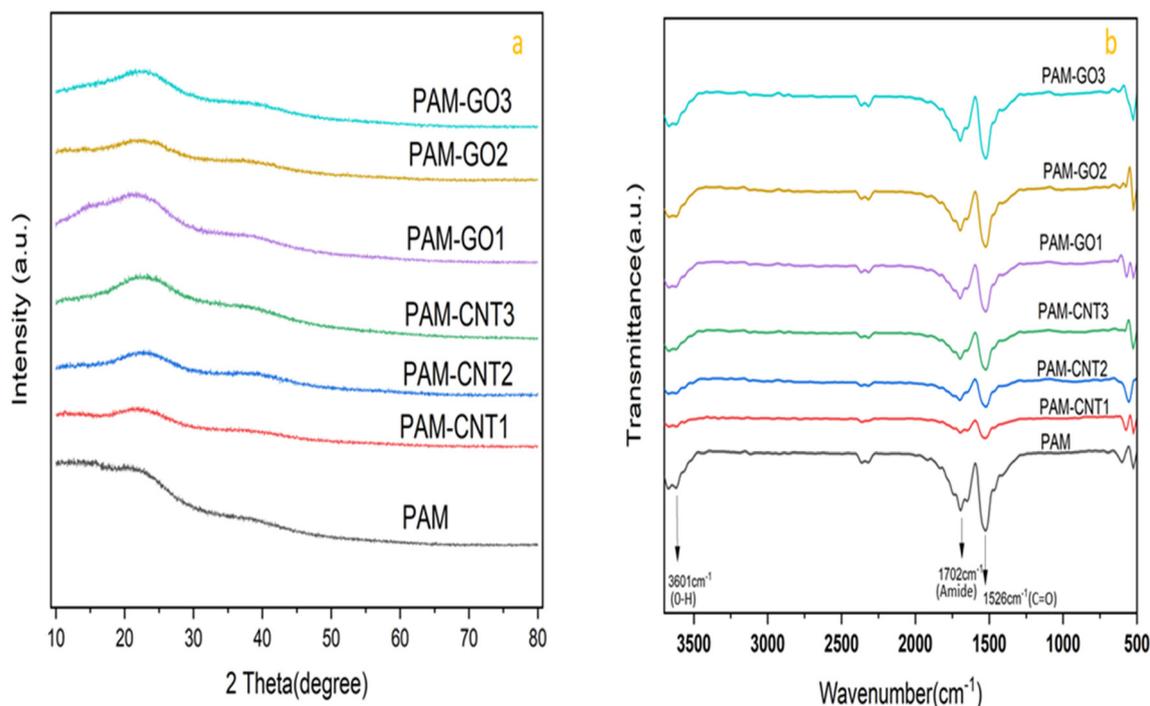
Fig. 3 (a) XRD pattern, (b) FT-IR spectrum for PAM, PAM–CNT1, PAM–CNT2, PAM–CNT3, PAM–GO1, PAM–GO2, and PAM–GO3 hydrogel composites.
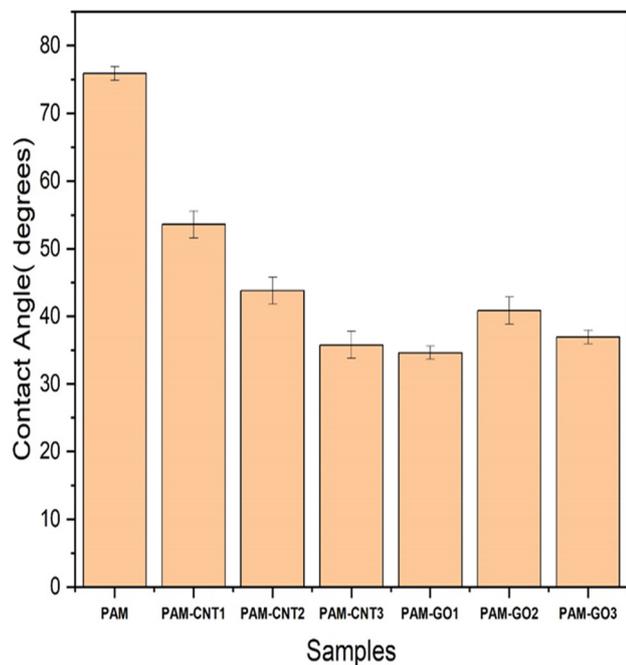

Fig. 4 Contact angle plot for PAM, PAM–CNT1, PAM–CNT2, PAM–CNT3, PAM–GO1, PAM–GO2, and PAM–GO3 hydrogel composites.

exceeds the ideal concentration, proving that 0.3 g L^{-1} GO provides the best-balanced reinforcement. The resulting stress–strain curves exhibit the distinctive "J-shaped" profile found in

natural ligaments and tendons. The PAM–GO1 composite created in this study has a significantly higher load-bearing capability than the chitosan–polyacrylamide hydrogels examined by Rosova *et al.* (2025), who reported a compressive strength of roughly 0.019 MPa in the swelled condition.[29] The compressive strength obtained in this study also surpasses those reported for previous PAM-based hydrogels (*e.g.*, 0.15 MPa by Ohsedo *et al.*), confirming superior mechanical reinforcement.[30] A mineralized PAM hydrogel was created by Hu *et al.* (2023) for use in subchondral bone applications. They found that the hydrogel had a compressive strength of 290 ± 30 kPa (0.29 MPa) while wet, which suggests that the mineral inclusion provided moderate reinforcement.[31] However, the PAM–GO1 hydrogel created in this work had greater compressive strength, indicating that graphene oxide offers superior load transfer and interfacial reinforcement in the PAM matrix. Similar to this, Wu *et al.* (2024) created poly (vinyl alcohol)/polyacrylamide (PVA/PAM) double-network hydrogels, which, depending on the network composition and testing parameters, achieved compressive stresses between 0.065 and 0.20 MPa.[32] When compared to dual-network techniques alone, these values are noticeably lower than those found in the current work, highlighting the fact that nanofiller-mediated interactions, specifically through oxygenated groups in GO, significantly improve mechanical resilience. In contrast to the natural mechanical performance of human articular cartilage, which generally has a compressive modulus between 0.5 and 1 MPa,[33] the PAM–GO1 hydrogel that was created shows mechanical compatibility in the lower physiological range. This
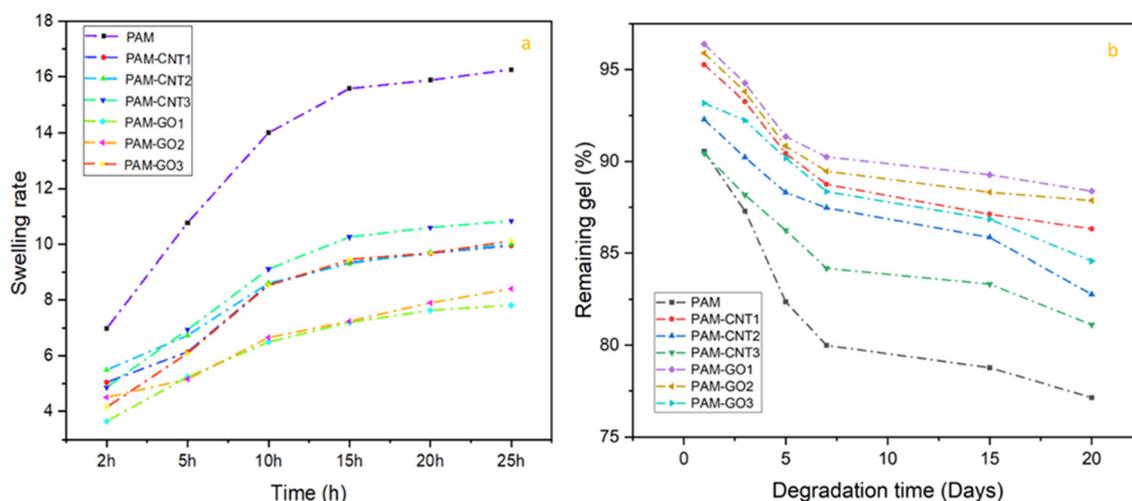
Fig. 5 (a) Swelling rate. (b) Degradation behaviour for PAM, PAM–CNT1, PAM–CNT2, PAM–CNT3, PAM–GO1, PAM–GO2, and PAM–GO3 hydrogel composites.
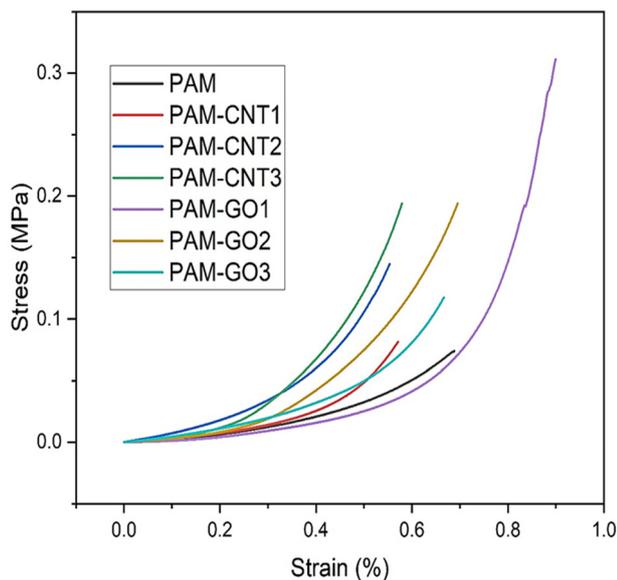

Fig. 6 Stress–strain curve for PAM, PAM–CNT1, PAM–CNT2, PAM–CNT3, PAM–GO1, PAM–GO2, and PAM–GO3 hydrogel composites.

compatibility with the characteristics of native tissue indicates that the optimized composite has enough elasticity and load-bearing capacity for possible uses in cartilage repair.

Elastic modulus measurements further supported this trend: PAM–GO1 exhibited an E_{high} of 1.653 ± 0.1, far exceeding the 0.23 MPa reported by Butylina *et al.* for nanocrystalline cellulose–PVA systems.[34]

3.4. Cytotoxicity assessment on the MG-63 cell line and antimicrobial analysis of hydrogels

The *in vitro* cytotoxicity of the nanocomposite hydrogels against the MG-63 cell line was assessed using the MTT test.

The synthesized reinforced hydrogels demonstrated cell viability of almost 100% (Fig. 7). The highest cell viability was for the PAM–GO3 hydrogel composite.[35] Hydrogels containing graphene oxide (GO) additives often enhance cell viability more than those using carbon nanotubes (CNTs). This results from GO's enhanced biocompatibility, surface functionalization, reduced cytotoxicity, improved dispersibility, and capacity to facilitate favourable cell–material interactions. Although carbon nanotubes can improve mechanical qualities, they provide increased risks of cytotoxicity and uneven dispersion, thereby compromising cell viability. The highest antimicrobial activity against *S. aureus* was found in PAM–GO1. The bacterial viability was very low in the sample (46.90 ± 3.55%). The fluorescence images (Fig. 8) show MG-63 cell adhesion and spread on the hydrogel surfaces after 72 h of incubation. F-actin filaments (green, Alexa Fluor 488-phalloidin) and nuclei (blue, DAPI) show a distinct cell shape and cytoskeletal organization in every sample (Fig. 8).

The bacterial viability of the samples reinforced with GO was significantly lower (40–50%) as compared to PAM. GO damages bacterial membranes through sharp edges and oxidative stress. At a low concentration, GO particles are well-dispersed, ensuring maximum exposure of GO nanosheets in bacterial cells, which results in direct contact-mediated bacterial killing.[36] The PAM–CNT1 composite showed the lowest bacterial viability (26 ± 3.2%) against *E. coli*, demonstrating higher antibacterial activity (Fig. 9). This is because CNTs have a better contact with the lipopolysaccharide-rich outer membrane of this Gram-negative bacterium.[37]

3.5. Computational modelling

Here in this research work, let us start our discussion by taking up three component models, the PAM chosen as the prime one, and two secondary components, the CNTCOOH
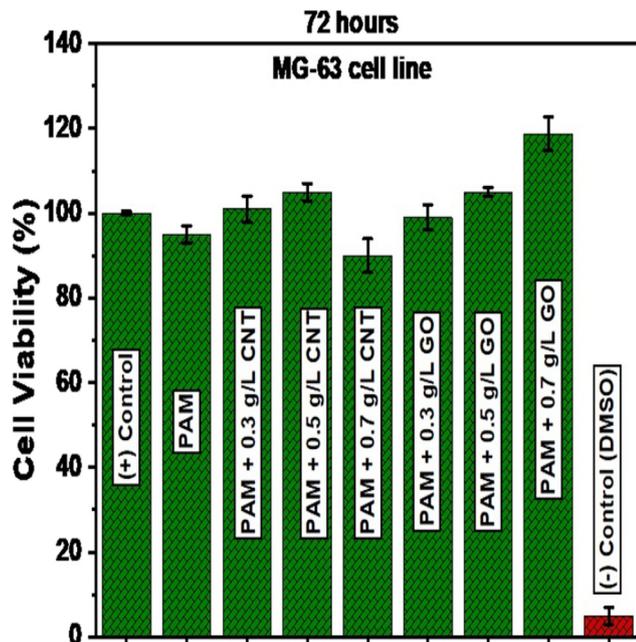
Fig. 7 MG-63 cell viability on composite hydrogel samples after 72 h culture.

and GO, which have been optimized with the employment of the *ab initio* and DFT approach, followed by *in silico* design using the molecular modelling approach (MMA). The optimized structures of all three constituting component models (PAM, GO, and CNTCOOH) can be seen in Fig. 10. Very interestingly, it has been found that all three components were self-stabilized due to having various intramolecular H-bonding interactions. Now, keeping in mind the executed experimental facets and the probable interfacial interactions found in the probed composites, two sets of three-dimensional composite models (PAM–GO and PAM–CNTCOOH) have been assembled by taking care of attaining the maximum number and strong interfacial interactions between the two constituting components (PAM and CNTCOOH for PAM–CNTCOOH as well as PAM and GO for PAM–GO). The optimized structures of two-body assembled systems, PAM–CNTCOOH and PAM–GO, can be viewed in Fig. 10 and 11, respectively.

The computational analysis was conducted to assess the interfacial interaction and electronic behaviour of the polymer-filler systems at the molecular level. All calculations were conducted utilizing the density functional theory framework, by specifically employing the HF/3-21G and B3LYP functional alongside the 6-31G* basis set (single point calculations) as executed. The geometries of the isolated polymer (PAM) and the filler models (CNT and GO) were initially refined to achieve their lowest energy configurations. Following this, the refined PAM-filler complexes underwent single-point energy calculations using the same theoretical framework. The binding energy (BE) of each complex was obtained using the expression:
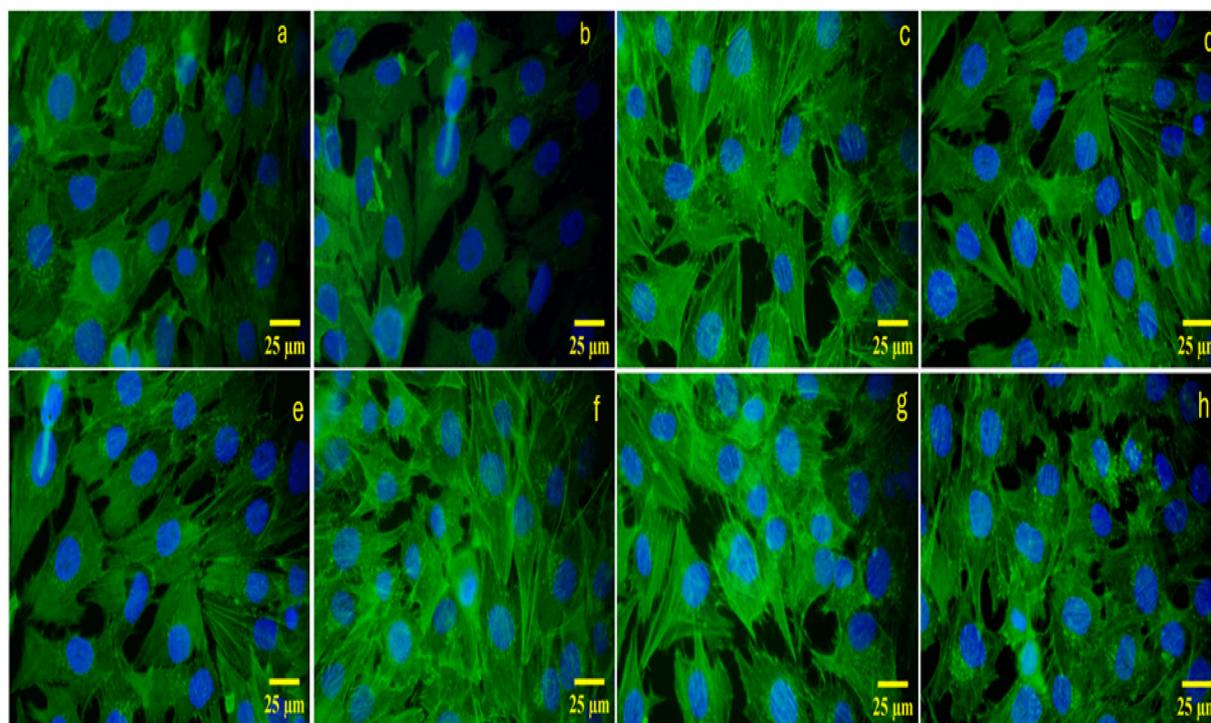
$$BE = E_{Complex} - (E_{PAM} - E_{Filler})$$

Fig. 8 Fluorescence microscopy images showing the MG-63 cells cultured on (a) untreated, (b) PAM, (c) PAM−CNT1, (d) PAM−CNT2, (e) PAM−CNT3, (f) PAM−GO1, (g) PAM−GO2, and (h) PAM−GO3 hydrogel samples.
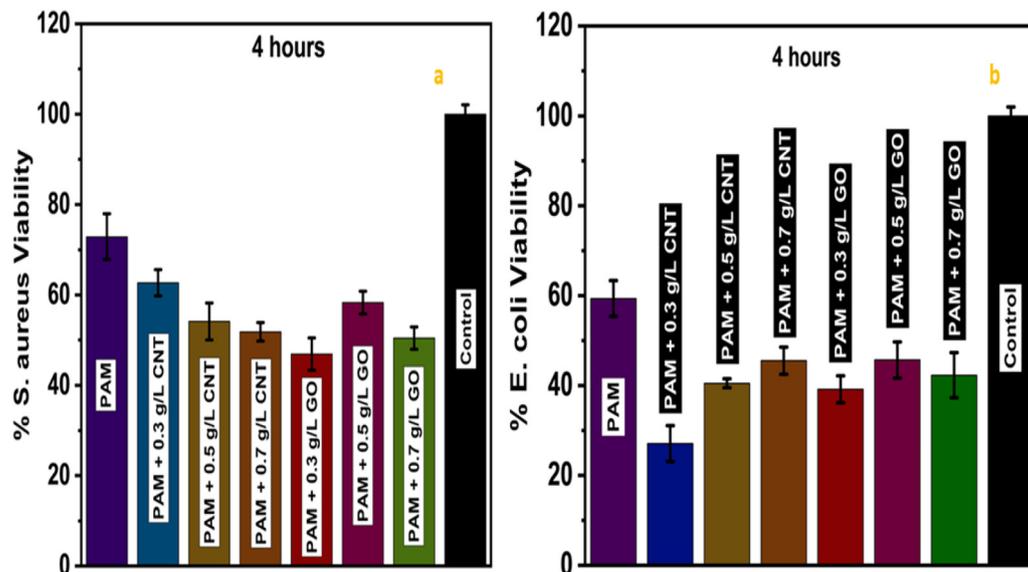
Fig. 9 Determination of the anti-bacterial activity of PAM, PAM−CNT1, PAM−CNT2, PAM−CNT3, PAM−GO1, PAM−GO2, and PAM−GO3 hydrogel composites in the presence of (a) *S. aureus* and (b) *E. coli*.
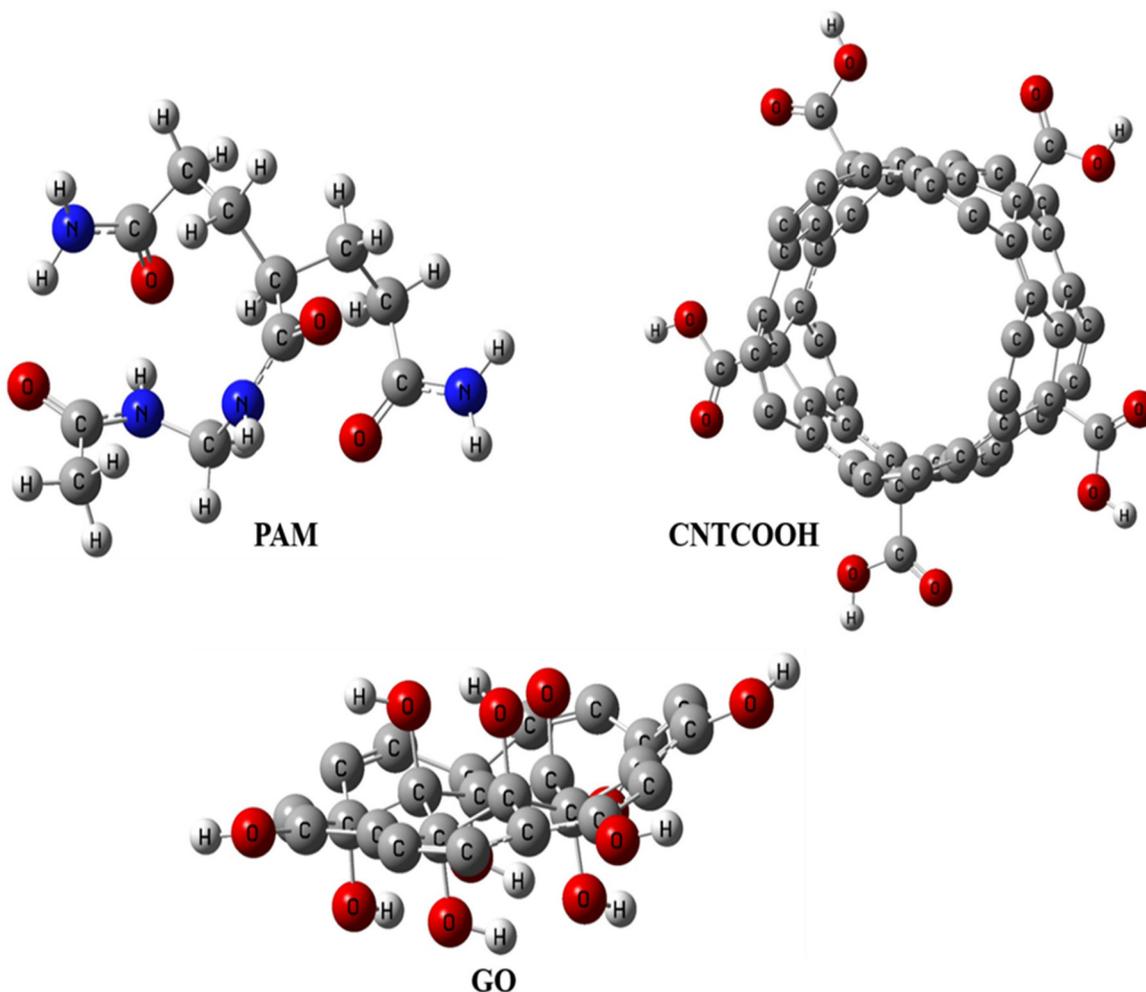

Fig. 10 Optimized/equilibrium structures of the PAM (top left), CNTCOOH (top right), GO (bottom) models at the B3LYP/6-31G* level of theory.

where E_{complex} is the total electronic energy of the optimized composite system, and E_{PAM} and E_{Filler} are the corresponding energies of the isolated components. A more negative binding energy indicates stronger interfacial interactions and higher thermodynamic stability of the composite.

The electronic characteristics of the systems were assessed through an analysis of the frontier molecular orbitals. The energy (E_{gap}) gap between the highest occupied and lowest unoccupied molecular orbitals (HOMOs and LUMOs) was determined, offering valuable insights into charge transfer and electronic conductivity. The dipole moment was derived directly from the DFT output and utilized to evaluate the

overall polarity of the system, indicating its potential for electrostatic and hydrogen-bonding interactions with the polymer matrix. Collectively, these parameters offer a numerical insight into the ways in which electronic interactions at the molecular level affect the overall performance of the composites.

Notably and very importantly, the binding energy (BE) calculations show that the PAM–GO composite is detected to be more stable than the PAM–CNTCOOG because the former one (PAM–GO) consists of a greater BE value than the latter one (PAM–CNTCOOH) using both approaches. Using the *ab initio* approach, the BEs of the PAM–GO and PAM–CNTCOOH are
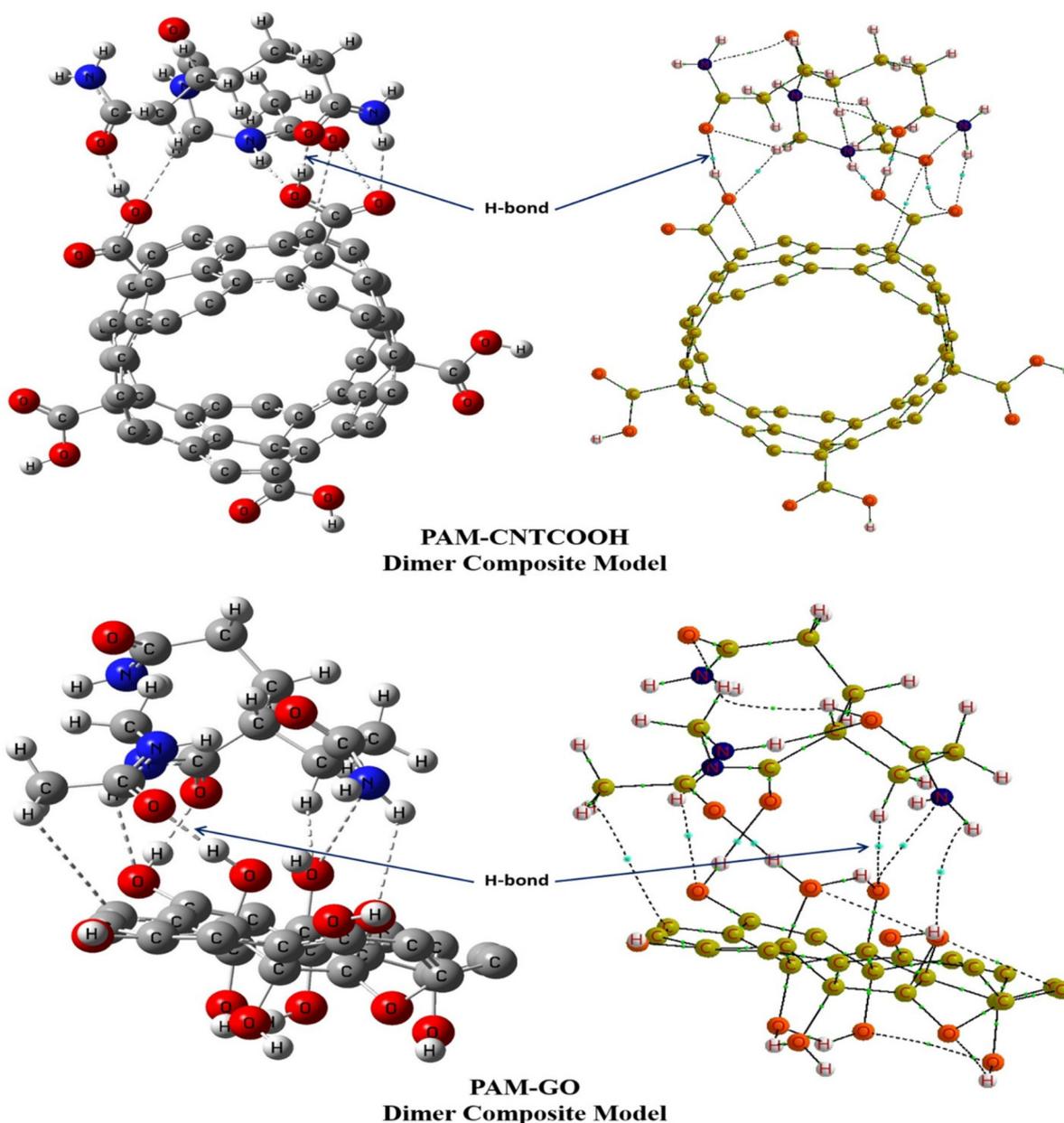
Fig. 11 Optimized structures (top, left) and QTAIM molecular graph (top, right) of the PAM−CNTCOOH and the optimized structures (bottom, left) and QTAIM molecular graph (bottom, right) of the PAM−GO composite models at the B3LYP/6-31G* level of theory.

Table 2 Elastic modulus at low and high strain and compressive strength of the PAM, PAM with CNTs (0.3 g L^{-1}), PAM with CNTs (0.5 g L^{-1}), PAM with CNTs (0.7 g L^{-1}), PAM with GO (0.3 g L^{-1}), PAM with GO (0.5 g L^{-1}), and PAM with GO (0.7 g L^{-1}) hydrogel composites

Samples	E_{low} (MPa)	E_{high} (MPa)	Compressive strength (MPa)	Maximum strain (%)
PAM	0.019 ± 0.01	0.297 ± 0.1	0.07	68
PAM–CNT1	0.024 ± 0.00	0.216 ± 0.1	0.08	57
PAM–CNT2	0.065 ± 0.01	1.808 ± 0.1	0.14	55
PAM–CNT3	0.029 ± 0.01	0.350 ± 0.1	0.07	66
PAM–GO1	0.018 ± 0.01	1.653 ± 0.1	0.31	90
PAM–GO2	0.027 ± 0.01	0.863 ± 0.1	0.19	69
PAM–GO3	0.029 ± 0.02	0.354 ± 0.1	0.07	66

calculated to be −44.7 kcal mol^{-1} and −28.1 kcal mol^{-1}, respectively, in which the stability of the former is 1.6 times that of the latter. Moreover, the BE outcomes provided a similar trend in the case of the DFT level of approach (PAM–GO: −60.4 kcal mol^{-1} and PAM–CNTCOOH: −14.8 kcal mol^{-1}), where the PAM–GO has been found to be 4.1 times more stable than the PAM–CNTCOOH system, which were also confirmed by the experimental observation. In order to validate the above trend, the bonding features have also been probed using the QTAIM tool. By having a look into the structural bonding in the PAM–CNTCOOH dimer composite, it has been probed that there is the existence of three kinds of conventional O–H···O, N–H···O, and weak C–H···O intermolecular H-bonding interactions including two types of extremely weak nonconventional nonbonding O···O and C···O (a diagnostic of stabilization) interactions. It is interesting to note that some of the atoms of the PAM component (O, N, and H atoms) interact with some of the atoms of the CNTCOOH (O, C, and H atoms) and create interfacial interactions which are responsible for stabilizing the dimer composite. Similarly, in the case of the PAM–GO system, three types of conventional O–H···O, N–H···O, and weak C–H···O interactions have been detected using the QTAIM-based technique including two kinds of extremely weak nonconventional C···H and N···O nonbonding stabilizing interactions. Some selected, useful, and calculated structural bonding parameters for both species are shown in

Table 3, which shows that the PAM–GO is more stable as compared to the PAM–CNTCOOH.

By having a look into the compressive strength given in Table 2 and the electronic parameters shown in Table 3, a detailed comparison has been highlighted. The DFT and experimental data together show that PAM–GO provides better reinforcement of the PAM matrix than PAM–CNT. Experimentally, PAM–GO exhibits a compressive strength of 0.31 MPa and a maximum strain of 90%, compared with 0.14 MPa and 55% for PAM–CNT, representing 121% and 64% improvements, respectively. The DFT calculations indicate that PAM–GO has a more negative binding energy (−60.4 kcal mol^{-1} vs. −14.8 kcal mol^{-1}), a slightly higher band gap (1.632 eV vs. 1.578 eV), and a lower dipole moment (3.3 D vs. 8.0 D). Moreover, the B3LYP/6-31G* (single-point calculations) indicates the binding energies of −44.7 kcal mol^{-1} for PAM–GO and −28.1 kcal mol^{-1} for the PAM–CNT, confirming substantially stronger interfacial interactions for GO (Δ = 16.6 kcal mol^{-1}). The higher binding energy of PAM–GO suggests stronger interfacial adhesion with the polymer matrix, which supports better stress transfer and mechanical stability. Although PAM–CNT shows a larger dipole moment, its weaker binding energy and poorer interfacial compatibility likely limit the load transfer efficiency. Consequently, both DFT and experimental evidence confirm that PAM–GO is the more effective reinforcing phase for PAM, offering improved strength and flexibility through enhanced interfacial bonding. So, PAM–GO has stronger binding and a slightly wider band gap, while the PAM–CNT has a higher dipole moment. Despite CNT's higher

Table 3 Binding energy (BE) and some important and selected electronic feature-based parameters of two composite models

Parameter	System	
	PAM–GO	PAM–CNTCOOH
BE (kcal mol^{-1}) using HF/3-21G	−60.4	−14.8
BE (kcal mol^{-1}) using B3LYP/6-31G*	−44.7	−28.1
B3LYP/6-31G(d)		
E_{HOMO} (eV)	−5.225	−5.143
E_{LUMO} (eV)	−3.701	−3.565
E_{gap} (eV)	1.632	1.578
Natural charge (Q)	Q_{PAM} (+0.124e)	Q_{PAM} (+0.110e)
	Q_{GO} (−0.124e)	$Q_{CNTCOOH}$ (−0.110e)
Dipole moment (Debye) of the composite model	3.3	8.0
Dipole moment (Debye) of the component model	PAM (3.9) GO (2.7)	PAM (3.9) CNTCOOH (0.7)

Table 4 Some chosen and important QTAIM topological parameters of the PAM–GO and PAM–CNTCOOH composite models

| Atoms	BPL (Å)	ρ (a.u.)	$\nabla^2(\rho)$ (a.u.)	$V(r)$ (kcal mol^{-1})	DI (A, B)
PAM–GO					
H36···O46	1.766	0.043	+0.136	−23.5	0.107
H43···O71	1.643	0.054	+0.175	−30.3	0.123
O35···H48	2.346	0.013	+0.047	−6.0	0.036
O40···H53	2.236	0.016	+0.053	−8.0	0.056
O42···H79	3.046	0.005	+0.022	−2.1	0.007
PAM–CNTCOOH					
H22···O104	2.501	0.008	+0.031	−3.7	0.028
H25···O100	2.090	0.021	+0.065	−11.2	0.060
H34···O99	2.064	0.022	+0.067	−11.3	0.065
O17···H105	1.661	0.050	+0.174	−28.3	0.114

dipole, the experimentally stronger and more flexible PAM–GO composite implies that the overall interfacial adhesion and dispersion are more effective with GO. Therefore, PAM–GO is the most preferable reinforcing phase when both high strength and large deformability are required. Combined DFT indicators (dipole moment and E_{gap}) and the measured mechanical improvements demonstrate that the PAM–GO shows superior interfacial compatibility and bulk mechanical performance relative to the PAM–CNT.

As shown in Table 4, some selected and useful QTAIM-based topological parameters describe the kind, nature, and strength of interfacial interactions involved therein, and the trend of the outcomes is consistent with the other theory-based earlier discussed results, as well as some data based on the experimental facets in terms of stability and strength. Fig. 11 illustrates the PAM–CNTCOOH and PAM–GO composite models, where the QTAIM analyzed molecular graphs are shown on the right side, and the interfacial interaction can clearly be seen through bond paths (BPs) indicated by black dotted lines consisting of small light greenish-blue spheres specifying the bond critical point (BCP). The ρ, $V(r)$, and DI (A, B) values show the strength of the interfacial NCIs, whereas the $\nabla^2(\rho)$ parameters indicate the nature of interactions. Here, all $\nabla^2(\rho)$ values are found to be positive and quite low, hence indicating closed-shell (contributing to a stable) NCI, often associated with H-bonds. On having a look at both structures, PAM–GO appeared to show more stability as compared to the PAM–CNTCOOH.

3.6. Frontier molecular orbital (FMO)

The highest occupied molecular orbital (HOMO) and lowest unoccupied molecular orbital (LUMO) and their difference (HOMO–LUMO gap, known as E_{gap}) obtained from the concept of the frontier molecular orbital (FMO) theory play a crucial role in predicting the stability/activity of any chemical species or materials.[38–40] A large energy gap (E_{gap}) between the HOMO and LUMO for a system shows the effective stability (less reactivity) of the system; in contrast, a smaller E_{gap} value indicates
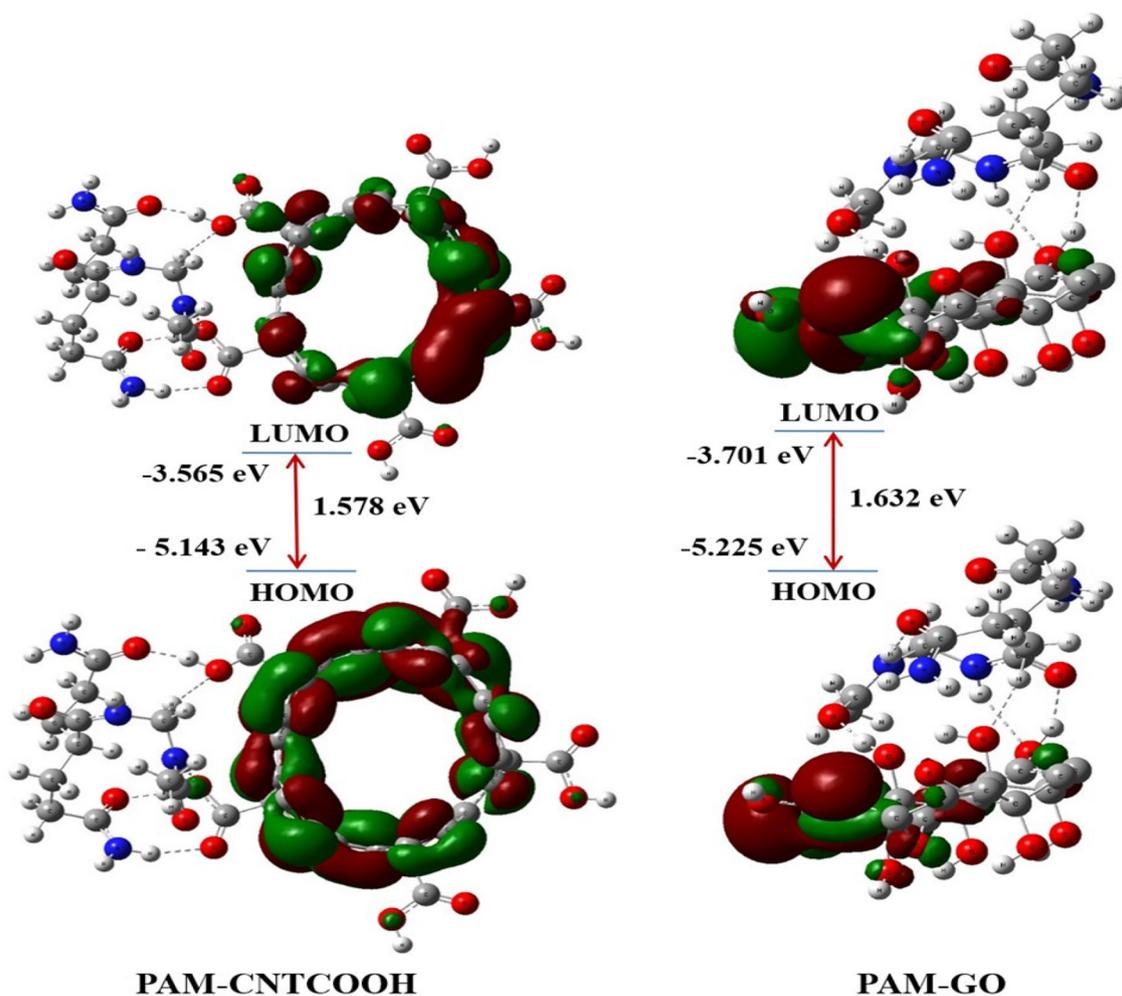
Fig. 12 The HOMO and LUMO 3D-isosurface maps of the PAM−CNTCOOH (left) and PAM−GO (right) dimer complexes at the B3LYP/6-31G(d) level of theory.

its higher chemical reactivity (less stability). Moreover, a higher HOMO value demonstrates the better electron-donating capability of the system, while a lower LUMO value indicates the better electron-accepting capability of any chemical to the biochemical system. Generally, the chemical hardness (a diagnostic of stability) of any material can also be assessed from the HOMO and LUMO parameters. The HOMO, LUMO, and HOMO–LUMO energy gap (E_{gap}) can be discerned from Table 3. The E_{gap} value of the PAM–GO composite (1.632 eV) is greater than that of the PAM–CNTCOOH system (1.578 eV), which gives the impression that the former one is more stable than the latter one, which is further supported by the BE values and CT observation along with some experimental strength/hardness-based data. Furthermore, and interestingly, the dipole moments of the individual components of the PAM–GO composite (PAM:

3.9 Debye and GO: 2.7 Debye) show that there is a chance of effective dipole–dipole interactions between both components as compared to the PAM–CNTCOOH composite (PAM: 3.9 Debye and CNTCOOH: 0.7 Debye).

Additionally, the three-dimensional HOMO–LUMO isosurface maps are given in Fig. 12 for both composite models. The HOMOs (in-phase) for the PAM-GO composite can be seen on one side (left side C atoms constituting pi-bonds) of the GO components, but the LUMOs (out-of-phase) are spread over almost the same regions. Finally, the HOMOs (in-phase) of the PAM-CNTCOOH are mainly located over the interfacial interaction side region, whereas the LUMOs (out-of-phase) are mainly distributed over the opposite side of the interfacial interaction region. Very interestingly, both composite models indicate the π to π* transition.
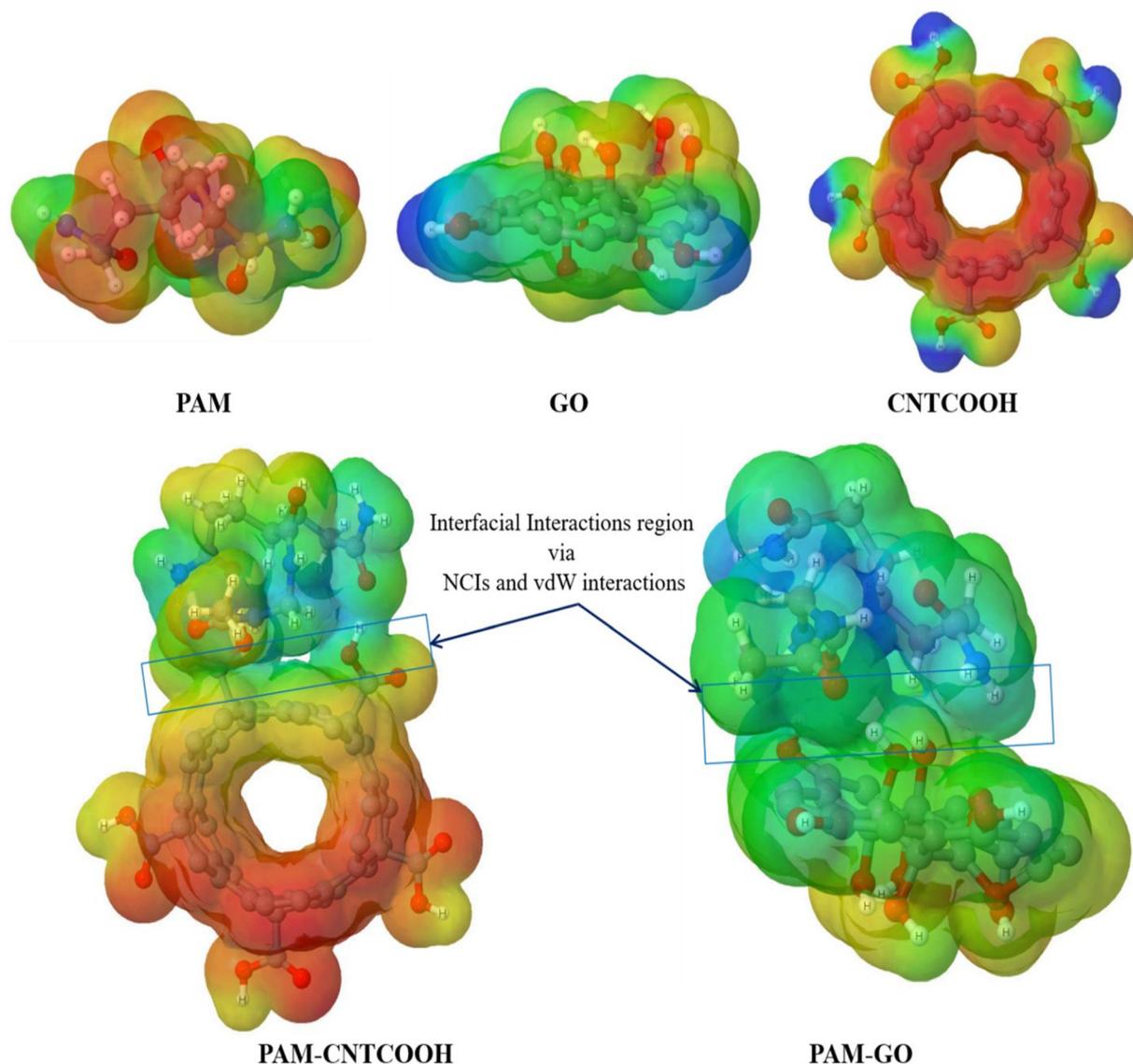

Fig. 13 The MESP plots of the component (PAM, GO, and CNTCOOH) (top) and dimer composite models (PAM–CNTCOOH, PAM–GO) (bottom).

3.7 Molecular electrostatic potential (MESP) surface

In attaining new insights into the size and shape of any chemical species and charge distributed over there, along with non-covalent interactions (NCIs) and chemical reactivity features, the molecular electrostatic potential (MESP) plot is well-connected with the electron density, which is one of the best ways for the recognition of any molecular system by another. The MESPs of all five species (three component and two composite models) can be seen in Fig. 13.

The electron-poor region (showing the reactive site for nucleophilic attack) is shown in a blue colour scheme (positive charge distribution); however, the red colour scheme indicates the electron-rich region (negative charge distribution), demonstrating the high probability of electrophilic attack at the reactive site. The orange colour scheme shows partially negatively charged regions. Moreover, the green colour scheme is diagnostic of neutral regions. In Fig. 11, the electronegative regions (suitable for electrophilic attack) are spread over the N and O atoms of the PAM, O of the GO, and O atoms as well as CNTs of the CNTCOOH components which are shown in red and orange colour schemes; however, the H-atoms are diagnostic of nucleophilic attack as shown in the blue or bluish-green colour scheme for the individual component models. A similar observation can be found for both composite models. The interfacial interaction (NCIs and vdW interactions) regions are shown by a rectangular box, where the MESP can clearly be seen in Fig. 11, and such observations were also validated by the supramolecular approach and the QTAIM tool.

3.8 Natural population analysis (NPA)

The natural population analysis (NPA) tool facilitates the charge (*i.e.* electron) populations of any atom contained by the chemical species, which are diagnostic of the charge distribution on the nuclei, bond order, *etc*. In this work, the NPA
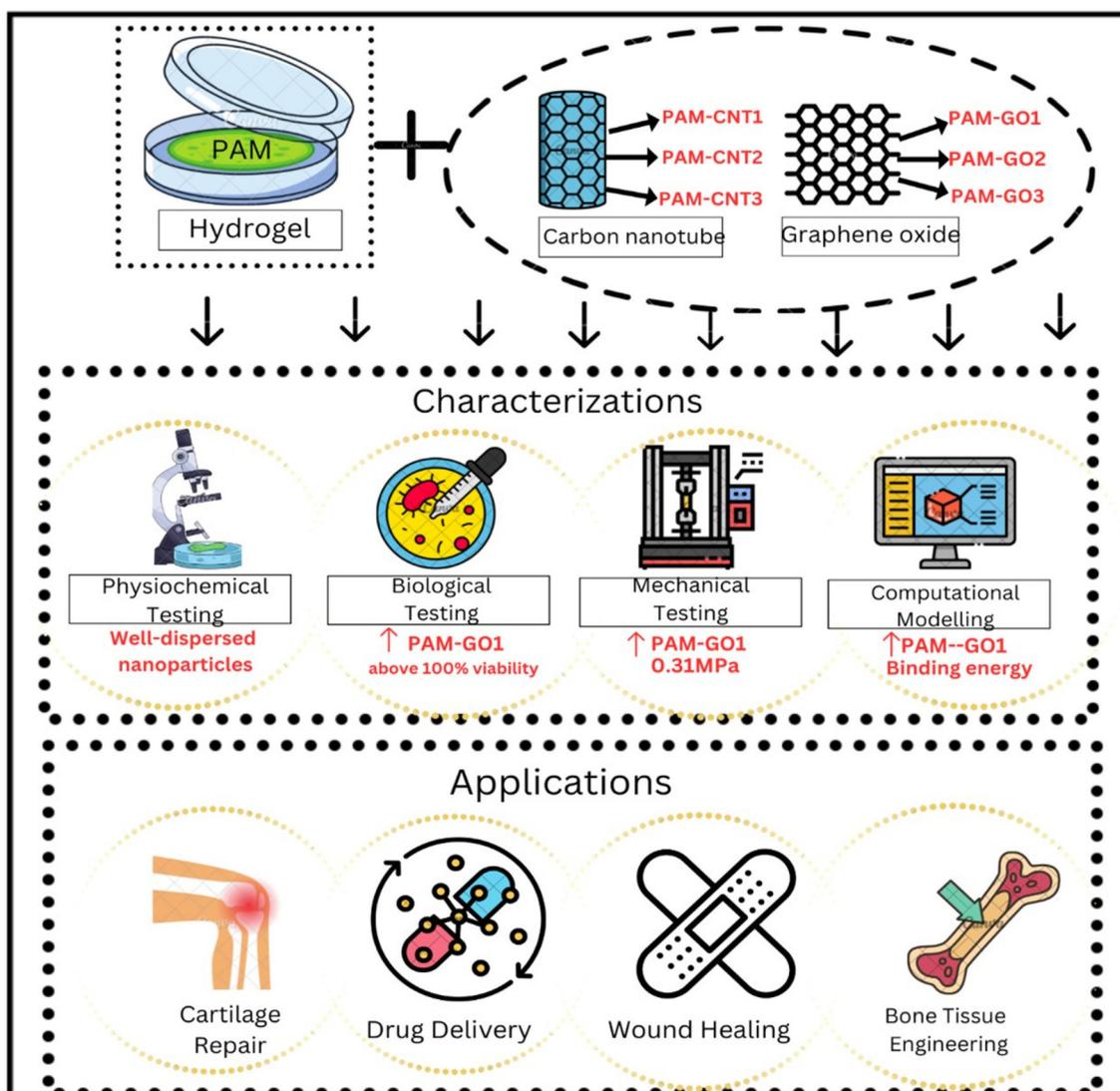

Fig. 14 Schematic representation of the application of nanoallotrope reinforced PAM using various theoretical and experimental studies.

technique was used to validate the stability trend of the PAM–GO and PAM–CNTCOOH by detecting the charge distribution on each component of the corresponding dimer composite models, along with visualization of three-dimensional MESP surface maps. Two two-component-based composite models show that the charge transfer (CT) takes place from PAM to CNTCOOH as well as from PAM to GO in the case of PAM–CNTCOOH and PAM–GO, respectively. The PAM–GO composite reveals that there is a slightly greater CT from PAM (Q_{PAM}: +0.124e) to GO (Q_{GO}: −0.124e) as compared to the PAM–CNTCOOH dimer composite (PAM$_Q$: +0.110e and $Q_{CNTCOOH}$: −0.110e), which strongly supports the supramolecular approach-based BE and electronic feature-based HOMO–LUMO gap (E_{gap}) trends of both composite models, demonstrating the stability pattern.

The strategic development of PAM-based hydrogel nanocomposites by including carbon nanotubes and graphene oxide derivatives is depicted in Fig. 14. Superior physicochemical dispersion, outstanding biocompatibility (particularly PAM–GO1 with >100% cell survival), improved mechanical characteristics (0.31 MPa for PAM–GO1), and advantageous binding interactions backed by computational modelling were all validated by thorough characterization. Altogether, our results support the promise of PAM–GO1 hydrogel systems for cutting-edge biomedical uses such as bone tissue creation, drug delivery, wound healing, and cartilage regeneration, opening the door for the development of next-generation multifunctional biomaterials.

4. Conclusion

The new hydrogel composites were prepared by the addition of CNTs and GO in different concentrations. The hydrophilicity of the composites was enhanced (contact angle = 40°) by reinforcing GO in the hydrogel matrix. The swelling rate was also discussed, and PAM–GO1 and PAM–GO2 hydrogel composites were found to be the most stable. The *in vitro* degradation behaviour was examined, and a higher amount of gel remained for PAM–GO1 and PAM–GO2 (∼90%) after 20 days of immersion in PBS. Furthermore, the mechanical strength of the prepared gels was investigated by a compression experiment, and it was concluded that PAM–GO1 had the highest compressive strength (≈0.31 MPa). Moreover, the synthesized PAM–GO hydrogels demonstrated cell viability of almost 100%. PAM–GO1 showed the highest antimicrobial activity. In conclusion, the PAM–GO1 hydrogel composite, characterized by enhanced mechanical characteristics, bioactivity, and strong adhesion, demonstrates significant potential as a next-generation hydrogel material for cartilage repair applications. Building on these discoveries, PAM–GO1's greater performance may be ascribed to graphene oxide's homogeneous dispersion within the polymer matrix, which enhanced the hydrogel's physical integrity and promoted advantageous interactions with biological tissues. Excellent cytocompatibility is indicated (100% cell viability), which makes it appropriate for bio-medical applications without producing harmful effects. Furthermore, by lowering the likelihood of post-implantation infections, a crucial need for regenerative medicine, the potent antibacterial qualities provide a dual benefit. Overall, GO incorporation significantly enhanced mechanical strength, hydrophilicity, cytocompatibility, and antibacterial activity, outperforming CNT-reinforced systems. The optimal GO concentration (0.3 g L^{-1}) achieved balanced flexibility and strength, making PAM–GO1 the most promising candidate for load-bearing cartilage repair applications. The findings confirm that strong interfacial bonding, uniform nanoparticle dispersion, and reduced water uptake are key factors governing the superior performance of PAM–GO hydrogels. The PAM–GO1 hydrogel showed promise as a possible scaffold material for cartilage tissue engineering *in vitro* by exhibiting improved mechanical strength, hydrophilicity, and cytocompatibility. Nevertheless, additional *in vivo* and long-term bioreactor research is necessary to confirm its clinical application and functional efficacy.

Conflicts of interest

The authors declare no conflict of interest.

Data availability

Data will be made available on reasonable request.

References

1 W. A. Laftah, S. Hashim and A. N. Ibrahim, Polymer Hydrogels: A Review, *Polym.-Plast. Technol. Eng.*, 2011, **50**(14), 1475–1486, DOI: 10.1080/03602559.2011.593082.

2 H. J. Chung and T. G. Park, Self-assembled and nanostructured hydrogels for drug delivery and tissue engineering, *Nano Today*, 2009, **4**(5), 429–437, DOI: 10.1016/j.nantod.2009.08.008.

3 W. A. Laftah, S. Hashim and A. N. Ibrahim, Polymer Hydrogels: A Review, *Polym.-Plast. Technol. Eng.*, 2011, **50**(14), 1475–1486, DOI: 10.1080/03602559.2011.593082.

4 Z. Ahmad, *et al.*, Versatility of Hydrogels: From Synthetic Strategies, Classification, and Properties to Biomedical Applications, *Gels*, 2022, **8**(3), 167, DOI: 10.3390/gels8030167.

5 S. Bashir, *et al.*, Fundamental Concepts of Hydrogels: Synthesis, Properties, and Their Applications, *Polymers*, 2020, **12**(11), 2702, DOI: 10.3390/polym12112702.

6 Y. Chen, *Properties and development of hydrogels*, in *Hydrogels Based on Natural Polymers*, Elsevier, 2020, pp. 3–16. DOI: 10.1016/B978-0-12-816421-1.00001-X.

7 U. S. K. Madduma-Bandarage and S. V. Madihally, Synthetic hydrogels: Synthesis, novel trends, and applications, *J. Appl. Polym. Sci.*, 2021, **138**(19), DOI: 10.1002/app.50376.

8 S. Awasthi, J. K. Gaur, M. S. Bobji and C. Srivastava, Nanoparticle-reinforced polyacrylamide hydrogel composites for clinical applications: a review, *J. Mater. Sci.*, 2022, **57**(17), 8041–8063, DOI: 10.1007/s10853-022-07146-3.

9 E. Olăreț, *et al.*, Nanostructured Polyacrylamide Hydrogels with Improved Mechanical Properties and Antimicrobial Behavior, *Polymers*, 2022, **14**(12), 2320, DOI: 10.3390/polym14122320.

10 M. Arjmandi and M. Ramezani, Mechanical and tribological assessment of silica nanoparticle-alginate-polyacrylamide nanocomposite hydrogels as a cartilage replacement, *J. Mech. Behav. Biomed. Mater.*, 2019, **95**, 196–204, DOI: 10.1016/j.jmbbm.2019.04.020.

11 S. Awasthi, Unveiling the development principles and mechanistic understanding of controlled drug delivery strategies for chronic bone defects and diabetic wound management, *Mater. Adv.*, 2025, **6**(17), 5831–5856, DOI: 10.1039/D5MA00490J.

12 P. Cools, *et al.*, Acrylic Acid Plasma Coated 3D Scaffolds for Cartilage tissue engineering applications, *Sci. Rep.*, 2018, **8**(1), 3830, DOI: 10.1038/s41598-018-22301-0.

13 A. Venkataraman, E. V. Amadi, Y. Chen and C. Papadopoulos, Carbon Nanotube Assembly and Integration for Applications, *Nanoscale Res. Lett.*, 2019, **14**(1), 220, DOI: 10.1186/s11671-019-3046-3.

14 J. Yi, G. Choe, J. Park and J. Y. Lee, Graphene oxide-incorporated hydrogels for biomedical applications, *Polym. J.*, 2020, **52**(8), 823–837, DOI: 10.1038/s41428-020-0350-9.

15 S. Awasthi and S. K. Pandey, Recent advances in smart hydrogels and carbonaceous nanoallotropes composites, *Appl. Mater. Today*, 2024, **36**, 102058, DOI: 10.1016/j.apmt.2024.102058.

16 L. Zhang, *et al.*, High strength graphene oxide/polyvinyl alcohol composite hydrogels, *J. Mater. Chem.*, 2011, **21**(28), 10399, DOI: 10.1039/c0jm04043f.

17 S. Awasthi, S. K. Pandey, J. K. Gaur and C. Srivastava, Load-bearing study and interfacial interactions of hydroxyapatite composite coatings for bone tissue engineering, *Mater. Chem. Front.*, 2022, **6**(24), 3731–3747, DOI: 10.1039/D2QM00898J.

18 S. Das, *et al.*, Graphene/MWCNT/copper-nanoparticle fabricated printed electrode for diclofenac detection in milk and drinking water: Electrochemical and in-silico analysis, *J. Mol. Liq.*, 2024, **411**, 125750, DOI: 10.1016/j.molliq.2024.125750.

19 A. Chakravorty, S. Das, A. A. Mini, S. Awasthi, S. K. Pandey and V. Raghavan, MXene-derived potassium titanate nano-ribbon-decorated electrode architecture for the detection of ciprofloxacin: development of a multipurpose sensing platform promoting One Health, *Mater. Adv.*, 2025, **6**(6), 2090–2109, DOI: 10.1039/D4MA01245C.

20 S. Awasthi, J. K. Gaur and M. S. Bobji, Advanced ferrogels with high magnetic response and wear resistance using carbon nanotubes, *J. Alloys Compd.*, 2020, **848**, 156259, DOI: 10.1016/j.jallcom.2020.156259.

21 L. Wang, *et al.*, Dimeric BODIPY Donors Based on the Donor–Acceptor Structure for All-Small-Molecule Organic Solar Cells, *ACS Appl. Energy Mater.*, 2024, **7**(23), 11195–11205, DOI: 10.1021/acsaem.4c02425.

22 T. Wei, *et al.*, Bulk heterojunction organic photovoltaic cells based on D–A type BODIPY small molecules as non-fullerene acceptors, *J. Mater. Chem. C*, 2022, **10**(35), 12776–12788, DOI: 10.1039/D2TC02497G.

23 R. Prabhakar and D. Kumar, Influence of Dopant Ions on the Properties of Conducting Polyacrylamide/Polyaniline Hydrogels, *Polym.-Plast. Technol. Eng.*, 2016, **55**(1), 46–53, DOI: 10.1080/03602559.2015.1055501.

24 S. Saber-Samandari and M. Gazi, Pullulan based porous semi-IPN hydrogel: Synthesis, characterization and its application in the removal of mercury from aqueous solution, *J. Taiwan Inst. Chem. Eng.*, 2015, **51**, 143–151, DOI: 10.1016/j.jtice.2015.01.013.

25 Y. L. Luo, C. H. Zhang, Y. S. Chen and W. Yang, Preparation and characterisation of polyacrylamide/MWCNTs nanohybrid hydrogels with microporous structures, *Mater. Res. Innovations*, 2009, **13**(1), 18–27, DOI: 10.1179/143307509X402138.

26 X. Wang, H. Hou, Y. Li, Y. Wang, C. Hao and C. Ge, A novel semi-IPN hydrogel: Preparation, swelling properties and adsorption studies of Co(II), *J. Ind. Eng. Chem.*, 2016, **41**, 82–90, DOI: 10.1016/j.jiec.2016.07.012.

27 X. Wang, H. Hou, Y. Li, Y. Wang, C. Hao and C. Ge, A novel semi-IPN hydrogel: Preparation, swelling properties and adsorption studies of Co(II), *J. Ind. Eng. Chem.*, 2016, **41**, 82–90, DOI: 10.1016/j.jiec.2016.07.012.

28 R. A. McBath and D. A. Shipp, Swelling and degradation of hydrogels synthesized with degradable poly(β-amino ester) crosslinkers, *Polym. Chem.*, 2010, **1**(6), 860, DOI: 10.1039/c0py00074d.

29 E. Rosova, *et al.*, Preparation and Characterization of Biocompatible Hydrogels Based on a Chitosan-Polyacrylamide Copolymer, *Biomater. Connect*, 2025, **2**(1), 1, DOI: 10.69709/BIOMATC.2025.108000.

30 Y. Ohsedo, M. Taniguchi, K. Saruhashi and H. Watanabe, Improved mechanical properties of polyacrylamide hydrogels created in the presence of low-molecular-weight hydrogelators, *RSC Adv.*, 2015, **5**(109), 90010–90013, DOI: 10.1039/C5RA16823F.

31 Y. Hu, *et al.*, High biocompatible polyacrylamide hydrogels fabricated by surface mineralization for subchondral bone tissue engineering, *J. Biomater. Sci., Polym. Ed.*, 2023, **34**(16), 2217–2231, DOI: 10.1080/09205063.2023.2230856.

32 Z. Wu, *et al.*, Poly(vinyl alcohol)/polyacrylamide double–network ionic conductive hydrogel strain sensor with high sensitivity and high elongation at break, *J. Polym. Sci.*, 2024, **62**(20), 4599–4611, DOI: 10.1002/pol.20240209.

33 V. C. Mow, A. Ratcliffe and A. Robin Poole, Cartilage and diarthrodial joints as paradigms for hierarchical materials and structures, *Biomaterials*, 1992, **13**(2), 67–97, DOI: 10.1016/0142-9612(92)90001-5.

34 S. Butylina, S. Geng and K. Oksman, Properties of as-prepared and freeze-dried hydrogels made from poly(vinyl alcohol) and cellulose nanocrystals using freeze-thaw tech-

nique, *Eur. Polym. J.*, 2016, **81**, 386–396, DOI: 10.1016/j.eurpolymj.2016.06.028.

35 P. Picone, M. A. Sabatino, A. Ajovalasit, D. Giacomazza, C. Dispenza and M. D. Carlo, Biocompatibility, hemocompatibility and antimicrobial properties of xyloglucan-based hydrogel film for wound healing application, *Int. J. Biol. Macromol.*, 2019, **121**, 784–795, DOI: 10.1016/j.ijbiomac.2018.10.078.

36 S. Murab, S. Chameettachal and S. Ghosh, Establishment of an in vitro monolayer model of macular corneal dystrophy, *Lab. Invest.*, 2016, **96**(12), 1311–1326, DOI: 10.1038/labinvest.2016.102.

37 M. Asaftei, *et al.*, Fighting bacterial pathogens with carbon nanotubes: focused review of recent progress, *RSC Adv.*, 2023, **13**(29), 19682–19694, DOI: 10.1039/D3RA01745A.

38 S. K. Pandey, Novel and Polynuclear K- and Na-Based Superalkali Hydroxides as Superbases Better Than Li-Related Species and Their Enhanced Properties: An Ab Initio Exploration, *ACS Omega*, 2021, **6**(46), 31077–31092, DOI: 10.1021/acsomega.1c04395.

39 X. Zong, *et al.*, Alkynyl BODIPY-Core Bridged Perylene Diimide Star-Shaped Nonfullerene Acceptors for Efficient Polymer Solar Cells, *ACS Appl. Energy Mater.*, 2022, **5**(12), 15624–15637, DOI: 10.1021/acsaem.2c03200.

40 R. K. Mudsainiyan and S. K. Pandey, A Combined Theoretical Calculation and Hirshfeld Surface Analysis of Cooperative Non–covalent Interactions in the Crystal Packing in [Cu(L1)2 (EDA)], *Z. Anorg. Allg. Chem.*, 2017, **643**(20), 1245–1252, DOI: 10.1002/zaac.201700182.